Melting of Iron at Earth's Inner Core Boundary Based on Fast X-ray Diffraction

S. Anzellini,[1]* A. Dewaele,[1] M. Mezouar,[2] P. Loubeyre,[1] G. Morard[3]

Earth's core is structured in a solid inner core, mainly composed of iron, and a liquid outer core. The temperature at the inner core boundary is expected to be close to the melting point of iron at 330 gigapascal (GPa). Despite intensive experimental and theoretical efforts, there is little consensus on the melting behavior of iron at these extreme pressures and temperatures. We present static laser-heated diamond anvil cell experiments up to 200 GPa using synchrotron-based fast x-ray diffraction as a primary melting diagnostic. When extrapolating to higher pressures, we conclude that the melting temperature of iron at the inner core boundary is 6230 ± 500 kelvin. This estimation favors a high heat flux at the core-mantle boundary with a possible partial melting of the mantle.

Earth's inner core grows by solidification from the surrounding outer core, which is composed of molten iron (Fe) alloyed with ~10 weight percent light elements (1). Seismological data reveal important physical properties of the core, such as density (and hence pressure) and elasticity; however, they cannot directly reveal the corresponding temperature. Temperature in the core places important constraints on parameters like heat flux to the mantle, power for the geodynamo, and cooling rate, all of which are fundamental to Earth's heat budget and dynamics (2).

The temperature at the inner core boundary (ICB) is bracketed between the melting temperature of pure Fe at 330 GPa and the liquidus temperature of the outer core iron-rich alloy (3) [expected to be depressed by ~700 K (4)]. Neither dynamic (5–7) and static (8–11) compression measurements nor thermodynamic modeling (12–15) have resulted in a consensus ICB melting temperature, in part because these approaches suffer from intrinsic uncertainties. Dynamic measurements have long been considered the most promising way to determine the ICB temperature because shocked Fe melts around 230 GPa, yet the temperature determination (spanning from 5100 K to 6350 K) and the possibility of superheating in shock compression (16) are major uncertainties. Using laser heating in static diamond anvil cell (DAC) experiments to produce reliable melting data above 100 GPa is also difficult because of uncertainties in the pyrometric temperature measurements (17), the criterion used to identify the melting (18), and the possible temperature-induced chemical reactions (18, 19). In fact, estimation of Fe melting temperature at ICB pressure

based on static compression data spans the range 4850 (8) to 7600 K (10). Finally, the tremendous advances in computational capacity have enabled quantum-mechanics calculations of the melting behavior, but each method has underlying approximations or assumptions. For instance, melting temperatures from 6370 (14) to 7050 K (12) have been obtained with the same melting criterion— the coexistence of a liquid and solid phase in a molecular dynamics run—but a different description of interatomic forces within density functional theory. Going beyond density functional theory

with a quantum Monte Carlo simulation, melting was obtained at 6900 K (15) at 330 GPa.

Here, we report the laser-heated DAC determination of the Fe melting curve from 50 to 200 GPa, using a μm-spatial and s-time-resolved approach that has recently been applied to the determination of the Ta melting line (18). Fast x-ray diffraction (XRD) is used as the primary technique for structural determination. This approach presents several advantages: (i) The structural evolution of Fe can be followed during heating; (ii) the measured volume expansion of solid Fe provides an independent control of temperature measurements; (iii) chemical reactions, if any, can be observed within the few percentage detection limits; and (iv) most importantly, an unambiguous bulk signature of melting—i.e., the appearance of a diffuse ring—is recorded (9, 20). This technique offers an alternative to the melting diagnostics used in the past in the laser-heated DAC: motion of the sample surface (8, 10), microscopic observation of the recovered samples (10), and plateaus/drops on the temperature ramps (8, 21).

The XRD spectra obtained during heating provide direct information about the physical state of the laser-heated sample that can be correlated with additional information such as temperature T versus time (Fig. 1). From this, we determined that ε-Fe (hexagonal close packed) and γ-Fe (face-centered cubic) are the only structures observed in the investigated pressure-temperature range. This confirms earlier findings of a large stability field for ε-Fe (19, 22) and extends in
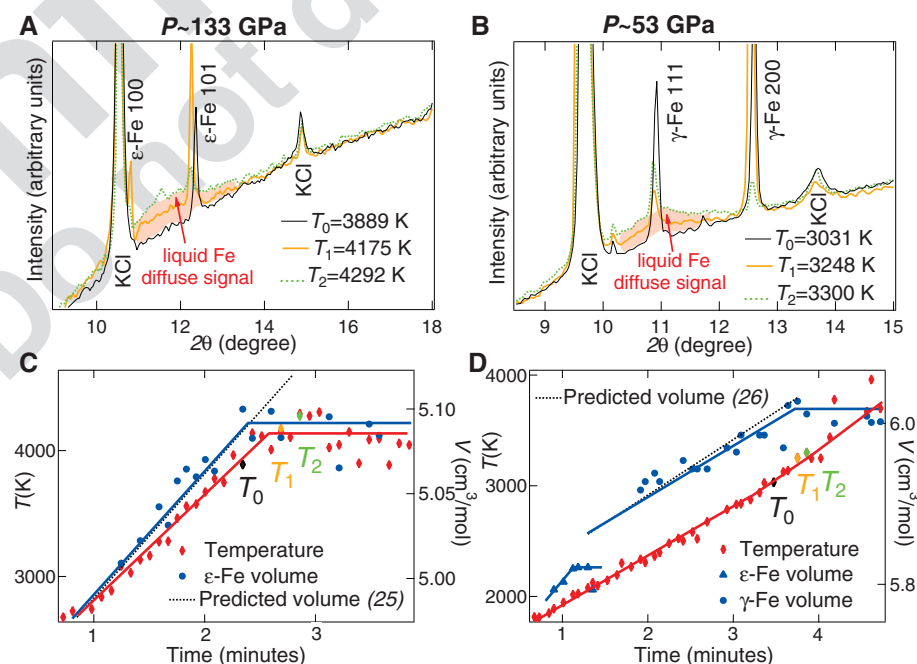

Fig. 1. XRD patterns as a function of temperature, pressure, and time. (**A** and **B**) XRD patterns of a ≈3-μm-thick (≈7-μm-thick) sample during a heating series at $P \approx 133$ GPa (A) and 53 GPa (B), respectively, recorded at different temperatures. γ-Fe, ε-Fe, and KCl pressure medium diffraction peaks are labeled. Liquid Fe is evidenced by a diffuse ring at $2\theta = 10°$ to $13.5°$. (**C** and **D**) Pyrometry temperature, measured and predicted (25, 26). Fe volume as a function of time for the thin (C) and thick (D) samples. The laser's power is linear with time. Data are in table S1.

[1]CEAxxxxx xxxxxxxxx xxxxxxxxx, DAMxxxxx xxxxxxxxxxxx xxx-xxxxxx, DIFxxxxxxxx xxxxx xxxxxxxx, 91297 Arpajon Cedex, France. [2]European Synchrotron Radiation Facility, BP 220, F-38043 Grenoble Cedex, France. [3]IMPMCxxxxxxxx xxxxxxxxx xxxxxxxxxxx xxxxxxxxxx xxxxxxx, UMR CNRS 7590, Université Pierre et Marie Curie, 75005 Paris, France.

*Corresponding author. E-mail: simone.anzellini@cea.fr

temperature this domain up to the melting line at 200 GPa—e.g., under the conditions where a transformation to a body-centered cubic phase had been suggested using shock wave measurements (23) or ab initio calculations (24). XRD patterns also show, in a few cases, a partial reaction of Fe with the diamond anvil, as shown by the appearance of weak peaks that can be assigned to Fe₃C (20). Therefore, each heating series was performed on a fresh, unheated zone of the sample. Furthermore, we measured and compared the volume of solid Fe with the expected volume based on the pyrometry temperature and the equation of state of ε-Fe (25) or γ-Fe (26), assuming that the

Fig. 2. Pressure (P_{KCl})–temperature conditions at which XRD patterns have been collected. Different symbols correspond to different Fe phases and textures. The continuous black lines correspond to Eqs. 1, 2, and 3. Data are in table S1.

Fig. 3. Phase stability domains for Fe obtained in the literature and in this study. The stability field for ε-Fe is based on the current study data and data from (19).

pressure remained constant. In cases where an inconsistency was detected, the ramp data was discarded. Finally, XRD images yield information on the sample texture: The starting fine powder transformed into large single crystals upon heating. Above a certain temperature, single-crystal spots appeared and disappeared at each XRD exposure, which we refer to as "fast recrystallization."

Changes in T versus time curves, such as plateaus or sudden drops, are often considered as a melting signature (8, 21). This is interpreted as a loss of thermal insulation in the sample assembly due to melting (27). We observed such features, but not systematically. In Fig. 1, the temporal evolutions of the temperature and the ε-Fe volume of a ≈3-μm thickness sample are parallel: a linear increase, then a marked plateau. A diffuse scattering signal of the liquid appears in the XRD signal at the beginning of this plateau; however, ε-Fe single crystal XRD spots indicate that the sample is not completely molten. For a thicker (≈7 μm) sample, the observations seem less correlated. After the expected γ-Fe to ε-Fe phase transition (22), the ε-Fe volume has a similar behavior as for the thin sample: It plateaus during melting, evidenced by the diffuse XRD signal. However, the pyrometry temperature continues to increase. With the rise of temperature, the intensity of the liquid signals increases, indicating that the amount of molten Fe scanned by XRD increases. Our interpretation is that the solid Fe is surrounded by layer of liquid Fe a few μm thick, whose surface is heated and analyzed by pyrometry. We observe that this layer sustains a sharp temperature gradient, its surface being up to 400 K warmer than solid Fe. The XRD measurement of the plateau of thermal expansion and the simultaneous observation of the diffuse diffraction peak of the liquid provide here an unambiguous signature of melting.

The melting temperature T_m is estimated as the average between, respectively, the highest (lowest) temperatures at which only solid (solid + liquid) Fe is observed (Fig. 2). The temperature of fast recrystallization is substantially (400 to 900 K) lower than the melting temperature. Two Simon equations are used to fit the melting points together with existing low-pressure data (28). The ε-Fe to γ-Fe phase boundary is estimated using the current data and literature data (22, 28). The γ-ε-liquid triple point is at 98.5 GPa (P_{TP}) and 3712 K (T_{TP}). The following formulations are obtained [T in K, P in GPa, T_0 = 1991 K, and P_0 = 5.2 GPa (28)].

$$T = 575 + 18.7P + 0.213P^2 - 0.000817P^3$$
$$(\varepsilon - Fe/\gamma - Fe) \qquad (1)$$
$$(P - P_0)/27.39 = (T_m/T_0)^{2.38} - 1$$
$$(\gamma - Fe/liquid) \qquad (2)$$
$$(P - P_{TP})/162.6 = (T_m/T_{TP})^{1.72} - 1$$
$$(\varepsilon - Fe/liquid) \qquad (3)$$

The present melting curve closely follows the one determined by Alfè et al. (13) on the basis of a Gibbs free-energy minimization (Fig. 3). It goes
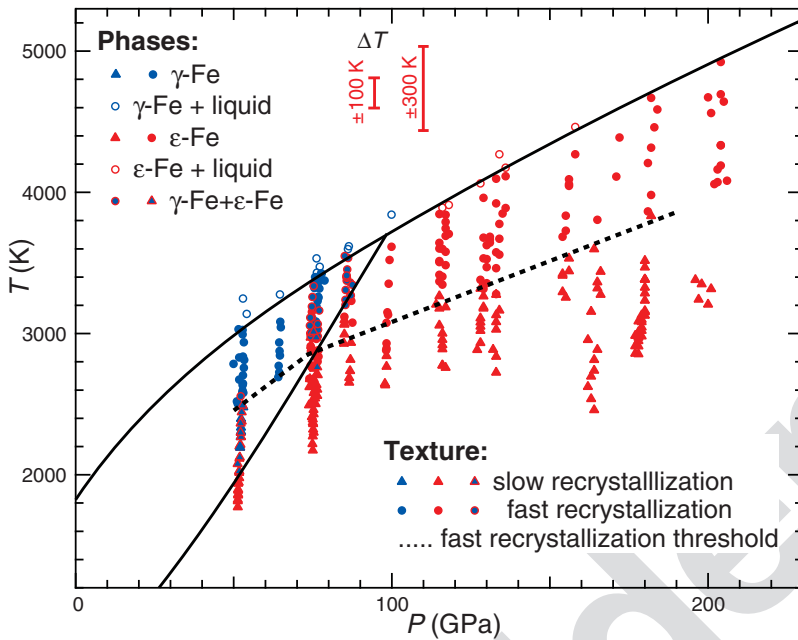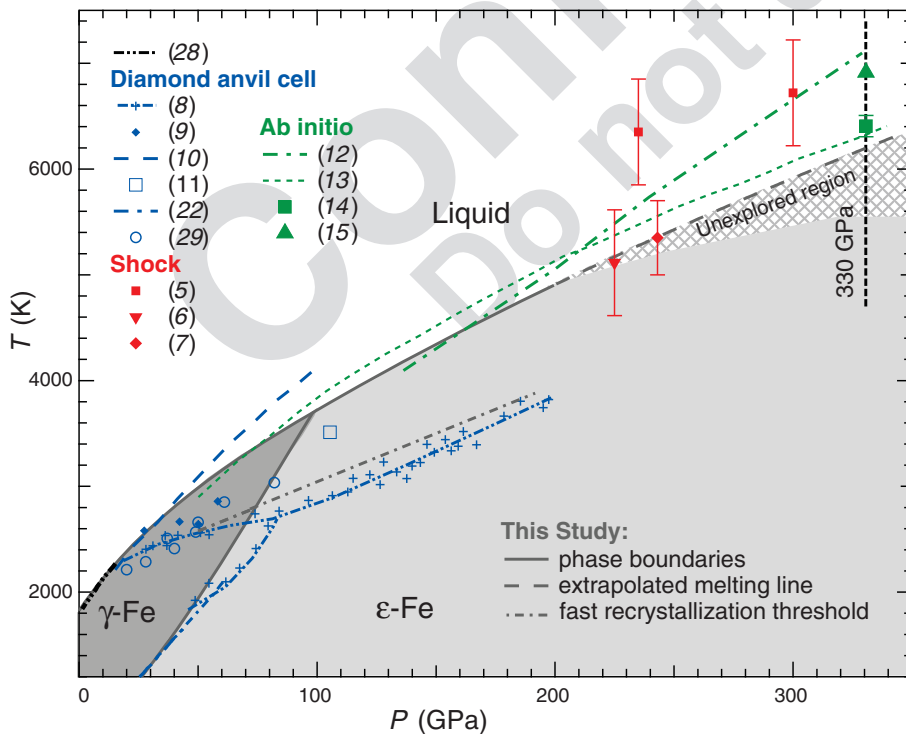
through the same dynamic determinations of melting as in (*6, 7*), around 230 GPa. The melting temperatures of Fe obtained with the laser-heated DAC are bracketed by two studies (*8, 10*), which mainly differ in their melting criteria. The present melting curve is within the standard error of the measurements based on the observation of textural changes on recovered samples up to 100 GPa (*10*)—a method which is probably not possible above that pressure—and agrees correctly with determinations based on a similar method (*9, 11*) and a recent indirect measurement (*29*). The current melting points are up to 1000 K higher than the melting points obtained by the observation of surface motion of a laser-heated sample (*8*). Neither temperature measurement techniques, which are similar, nor pressure calibration issues can explain such a difference. It is possible that the melting diagnostic used in (*8*) detects fast recrystallization instead of melting. Indeed, it is interesting to note that the melting line of (*8*) coincides with the temperature of fast recrystallization, observed in this study and in another recent work (*30*). In the latter study, it was interpreted as melting evidence. We propose instead that fast recrystallization begins at temperatures below melting and causes the surface motion observed in (*8*), which had been wrongly attributed to melting.

Eq. 3 extrapolates to $T_m(330 \text{ GPa}) = 6230 \pm 500$ K. The error is the sum of the maximum pyrometry error and the uncertainty on the detection of melting temperature (200 K). A temperature profile inside Earth's core can be estimated using this value, which leads to a temperature at the core-mantle boundary (T_{CMB}) of 4050 ± 500 K (*20*). This corresponds to a thermal boundary layer of ~1400 K at the base of the mantle and, subsequently, a high CMB heat flux (~10 TW) (*2*). Such a value is needed to sustain the geodynamo with recent estimate of the core conductivity (*31*). At CMB pressure, partial melting of the mantle material has been observed at 4180 ± 150 K (*32*) and would therefore be possible with strong geodynamical and geochemical implications. At 135 GPa, the post-perovskite phase is stable below 3520 ± 70 K for $MgSiO_3$ (*33*); a double-crossing scenario (*33*) is therefore compatible with the current T_{CMB}, given the error of experimental determinations.

Our experiments result in better agreement between calculations, and dynamic and static DAC approaches, and reduce uncertainty on the expected melting temperature of Fe at the ICB pressure. Because this study spans the 50 to 205 GPa range, we cannot rule out the possibility of a phase transition in Fe at higher *P-T* (unexplored region in Fig. 3), that could slightly change the extrapolation of the current determination of the Fe melting curve.

References and Notes

1. J. P. Poirier, *Phys. Earth Planet. Inter.* **85**, 319 (1994).
2. T. Lay, J. Hernlund, B. A. Buffett, *Nat. Geosci.* **1**, 25 (2008).
3. D. Gubbins, B. Sreenivasan, J. Mound, S. Rost, *Nature* **473**, 361 (2011).
4. D. Alfè, M. J. Gillan, G. D. Price, *Contemp. Phys.* **48**, 63 (2007).
5. C. S. Yoo, N. C. Holmes, M. Ross, D. J. Webb, C. Pike, *Phys. Rev. Lett.* **70**, 3931 (1993).
6. J. H. Nguyen, N. C. Holmes, *Nature* **427**, 339 (2004).
7. J. M. Brown, R. G. McQueen, *J. Geophys. Res.* **91**, (B7), 7485 (1986).
8. R. Boehler, *Nature* **363**, 534 (1993).
9. G. Shen, V. B. Prakapenka, M. L. Rivers, S. R. Sutton, *Phys. Rev. Lett.* **92**, 185701 (2004).
10. Q. Williams, R. Jeanloz, J. Bass, B. Svendsen, T. J. Ahrens, *Science* **236**, 181 (1987).
11. Y. Ma *et al.*, *Phys. Earth Planet. Inter.* **143-144**, 455 (2004).
12. A. B. Belonoshko, R. Ahuja, B. Johansson, *Phys. Rev. Lett.* **84**, 3638 (2000).
13. D. Alfè, G. D. Price, M. J. Gillan, *Phys. Rev. B* **65**, 165118 (2002).
14. D. Alfè, *Phys. Rev. B* **79**, 060101 (2009).
15. E. Sola, D. Alfè, *Phys. Rev. Lett.* **103**, 078501 (2009).
16. S. N. Luo, T. J. Ahrens, *Phys. Earth Planet. Inter.* **143-144**, 369 (2004).
17. Q. Williams, E. Knittle, R. Jeanloz, *J. Geophys. Res.* **96**, (B2), 2171 (1991).
18. A. Dewaele, M. Mezouar, N. Guignot, P. Loubeyre, *Phys. Rev. Lett.* **104**, 255701 (2010).
19. S. Tateno, K. Hirose, Y. Ohishi, Y. Tatsumi, *Science* **330**, 359 (2010).
20. Materials and methods are available as supplementary materials on *Science* Online.
21. R. Boehler, N. Vonbargen, A. Chopelas, *J. Geophys. Res.* **95**, (B13), 21731 (1990).
22. T. Komabayashi, Y. Fei, Y. Meng, V. Prakapenka, *Earth Planet. Sci. Lett.* **282**, 252 (2009).
23. J. M. Brown, *Geophys. Res. Lett.* **28**, 4339 (2001).
24. A. B. Belonoshko, R. Ahuja, B. Johansson, *Nature* **424**, 1032 (2003).
25. A. Dewaele *et al.*, *Phys. Rev. Lett.* **97**, 215504 (2006).
26. T. Komabayashi, Y. Fei, *J. Geophys. Res.* **115**, (B3), B03202 (2010).
27. Z. M. Geballe, R. Jeanloz, *J. Appl. Phys.* **111**, 123518 (2012).
28. L. J. Swartzendruber, *Bull. Alloy Phase Diagr.* **3**, 161 (1982).
29. J. M. Jackson *et al.*, *Earth Planet. Sci. Lett.* **362**, 143 (2013).
30. R. Boehler, D. Santamaria-Pérez, D. Errandonea, M. Mezouar, *J. Phys. Conf. Ser.* **121**, 022018 (2008).
31. M. Pozzo, C. Davies, D. Gubbins, D. Alfè, *Nature* **485**, 355 (2012).
32. G. Fiquet *et al.*, *Science* **329**, 1516 (2010).
33. S. Tateno, K. Hirose, N. Sata, Y. Ohishi, *Earth Planet. Sci. Lett.* **277**, 130 (2009).

MS no: RE1233514/CJH/GEOCHEM PHYS